


Article

# Charge Trapping and Emission during Bias Temperature Stressing of Schottky Gate GaN-on-Silicon HEMT Structures Targeting RF/mm Wave Power Amplifiers

Barry O'Sullivan <sup>1,\*</sup>, Aarti Rathi <sup>1</sup>, Alireza Alian <sup>1</sup>, Sachin Yadav <sup>1</sup>, Hao Yu <sup>1</sup>, Arturo Sibaja-Hernandez <sup>1</sup>, Uthayasankaran Peralagu <sup>1</sup> , Bertrand Parvais <sup>1,2</sup>, Adrian Chasin <sup>1</sup> and Nadine Collaert <sup>1,2</sup>

<sup>1</sup> IMEC, Kapeldreef 75, 3001 Leuven, Belgium

<sup>2</sup> Faculty of Engineering, Vrije Universiteit Brussel, 1050 Ixelles, Belgium

\* Correspondence: barry.osullivan@imec.be

**Abstract:** For operation as power amplifiers in RF applications, high electron mobility transistor (HEMT) structures are subjected to a range of bias conditions, applied at both the gate and drain terminals, as the device is biased from the OFF- to ON-state conditions. The stability of the device threshold voltage ( $V_t$ ) condition is imperative from a circuit-design perspective and is the focus of this study, where stresses in both the ON and OFF states are explored. We see rapid positive threshold voltage increases under negative bias stress and subsequent recovery (i.e.,  $V_t$  reduces), whereas conversely, we see a negative  $V_t$  shift under positive stress and  $V_t$  increase during the subsequent relaxation phase. These effects are correlated with the thickness of the GaN layer and ultimately result from the deep carbon-acceptor levels in the C-GaN back barrier incorporated to screen the buffer between the silicon substrate and the epitaxially grown GaN layer. Methods to mitigate this effect are explored, and the consequences are discussed.

**Keywords:** GaN on Si; Schottky gate HEMT; charge trapping; C-GaN back barrier



**Citation:** O'Sullivan, B.; Rathi, A.; Alian, A.; Yadav, S.; Yu, H.; Sibaja-Hernandez, A.; Peralagu, U.; Parvais, B.; Chasin, A.; Collaert, N. Charge Trapping and Emission during Bias Temperature Stressing of Schottky Gate GaN-on-Silicon HEMT Structures Targeting RF/mm Wave Power Amplifiers. *Micromachines* **2024**, *15*, 951. <https://doi.org/10.3390/mi15080951>

Academic Editor: Niall Tait

Received: 7 June 2024

Revised: 12 July 2024

Accepted: 23 July 2024

Published: 24 July 2024



**Copyright:** © 2024 by the authors. Licensee MDPI, Basel, Switzerland. This article is an open access article distributed under the terms and conditions of the Creative Commons Attribution (CC BY) license (<https://creativecommons.org/licenses/by/4.0/>).

## 1. Introduction

The quest for continued enhancements of internet speeds, with the advent of the Internet of Things, artificial intelligence, and virtual reality, requires evolutions in device technologies, and concurrently, device-to-device communications. Research is ongoing into technologies for application in the fifth generation of mobile networks (5G), which can operate at sufficient bandwidth and provide the communication speeds required for these applications. Such devices can operate within the frequency bands labeled as FR3 (~7–25 GHz) and FR2 (24–71 GHz) ranges, which have been assigned for communications. In these frequency ranges, it has been shown that GaN shows superior output power for frequencies up to 100 GHz, above which InP is more promising for the 6G node [1].

However, GaN substrates are produced in sizes up to 6" [2], but given the substrate costs, the intrinsic benefits of GaN, such as the high breakdown and high mobility potential, cannot be commercially exploited in this form. Research efforts are ongoing to integrate GaN on SiC substrates, which have lower costs than GaN substrates and are available in up to a 6" wafer size [3], or GaN on Si, which has been recently reported to have up to 200 mm [1] and 300 mm substrates diameters [4,5]. The scaling of these GaN on silicon technologies results in significant promise for millimetre wave applications, given that it could be integrated into streamlined silicon production facilities. However, given the lattice mismatch between the underlying SiC or Si substrate, the epitaxially grown GaN layers are prone to significant densities of defects [6]. Efforts to mitigate these defect regions' impact include inserting thick buffer layers and back-barrier layers. While the effect of the defects can be screened by these, in the case of back barriers, AlGaIn and C-GaN are frequently applied, which introduce their own challenges, including the lower thermal conductivity of

AlGaN, resulting in self-heating challenges [7], whereas the carbon-doping level in p-type C-GaN [8] can interact with, and degrade the device's operation [9].

During operation in class AB, power-amplifier devices are subjected to varying drain and gate biases ( $V_d$  and  $V_g$ , respectively), resulting in the application of bias when the device could be biased in the OFF state (negative  $V_g$ ), semi-on state (moderate  $V_g$ , moderate  $V_d$ ), ON-state (high  $V_g$ , low  $V_d$ ), or an intermediate zone between these. The impact of ON-state stress on  $R_{on}$  dispersion of Schottky gate structures has been explored [10–12] and shown to be related to charge trapping in AlGaN barrier defects, GaN/buffer defects, and AlGaN/SiN surface states.

In this work, we explore the region of low drain and varying gate bias stressing and study the charge trapping and emission characteristics for a range of Schottky gate HEMT structures. We show a correlation with the distance between the 2DEG channel and the C-GaN back barrier on the threshold voltage shifts under both positive (similar to [13]) and negative gate bias stress. Due to the varied bias range applied in RF operation [14], insights into the underlying physical degradation mechanisms are critical and can more readily be learned from DC conditions, such as those performed in this study.

## 2. Materials and Methods

The starting materials were high-resistivity 200 mm Si substrates, onto which epitaxial GaN-based layers were monolithically integrated, as described in [15]. To screen the impact of the buffer layer and its inherent defectivity, a 1  $\mu\text{m}$  carbon-doped GaN back barrier was incorporated underneath the (unintentionally doped) GaN channel. This GaN channel thickness varied between 35 and 300 nm in this study. A thin AlN layer (1 nm) was deposited above the channel, followed by the 15 nm AlGaN barrier layer, which was passivated with a  $\text{SiN}_x/\text{Al}_2\text{O}_3$  stack. The gate region was defined by etching through the passivation layers and partially through the AlGaN barrier to create Schottky gate or HEMT structures. In this case, the final AlGaN thickness under the metal electrode was 8 nm. The polarization charge in the AlGaN/AlN creates a 2D electron gas (2DEG) at the GaN surface, and thus, these devices are in the on state when unbiased. To switch off the device, negative gate bias is applied, which in practice switches off the 2DEG under the gate to limit the source-drain current flow in depletion-mode (D-mode) devices. The dc and RF characteristics of these structures have previously been reported [15] and show that the thinner GaN channel shows improved drain-induced barrier lowering (DIBL),  $I_{off}$ , and  $V_t$  roll-off but also shows degraded RF parameters, including cutoff frequency ( $f_T$ ), maximum frequency ( $f_{max}$ ), power-added efficiency (PAE), thermal conductance, and charge trapping when biased in the semi-ON state.

In this study, variations are made in the GaN channel thickness, from 35 to 300 nm, together with the type of back barrier incorporated between the buffer layer and the channel. A schematic diagram of the HEMT structures explored is depicted in Figure 1, and the layer specifications applied are listed in Table 1.

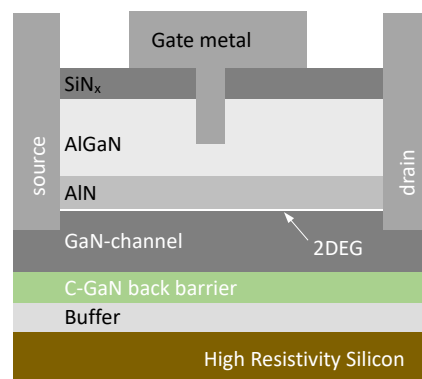


**Figure 1.** Schematic diagram of HEMT structures as applied in this work and fabricated on 200 mm silicon substrates.

**Table 1.** Process splits of GaN HEMT samples explored in this study.

Back Barrier	GaN Channel	AlN	AlGaIn
1 $\mu\text{m}$ C-GaN	300 nm	1 nm	15 nm $\rightarrow$ 8 nm
1 $\mu\text{m}$ C-GaN	150 nm	1 nm	15 nm $\rightarrow$ 8 nm
1 $\mu\text{m}$ C-GaN	100 nm	1 nm	15 nm $\rightarrow$ 8 nm
1 $\mu\text{m}$ C-GaN	50 nm	1 nm	15 nm $\rightarrow$ 8 nm
1 $\mu\text{m}$ C-GaN	35 nm	1 nm	15 nm $\rightarrow$ 8 nm
1 $\mu\text{m}$ C-GaN and 100 nm AlGaIn	35 nm	1 nm	15 nm $\rightarrow$ 8 nm
1 $\mu\text{m}$ C-GaN and 250 nm AlGaIn	35 nm	1 nm	15 nm $\rightarrow$ 8 nm

The transistor transfer and output characteristics are displayed in Figure 2 for the different GaN channel samples explored in this work. Clearly, the GaN channel thickness impacts the device threshold voltage and drain current and off-state leakage, as has previously been discussed [15] but are included here for reference.

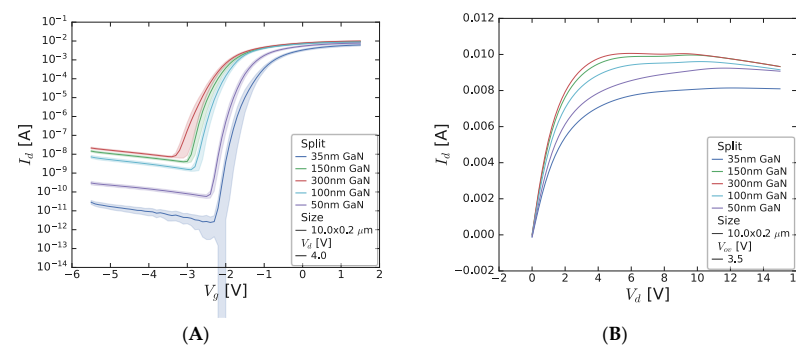


**Figure 2.** Transistor (A)  $I_d$ - $V_g$  and (B)  $I_d$ - $V_d$  characteristics measured on devices of drawn size  $10 \times 0.2 \mu\text{m}$  for a range of GaN thickness samples. In the case of the  $I_d$ - $V_g$ , the drain bias was 100 mV, while the  $V_d$  was 4 V for the  $I_d$ - $V_d$  curves.

The methodology of the charge-trapping measurements applied was as follows: the transfer characteristics of a reference device were measured to read the threshold voltage, and current at threshold condition, under a drain bias of 50 mV. Moving to the test device, the initial  $I_d$ - $V_g$  characteristics were recorded, with a current compliance incorporated, defined as double the drain current at the reference threshold current value, to ensure that the device was not stressed during the initial measurement stage. The evolution of the drain current was monitored intermittently during an applied stress voltage, with stress phases ranging in duration from  $\sim 30$  ms to 2 ks. After each stress phase, the time evolution of the drain current was measured, also from ms to ks range and, using the initial IV characteristics, transformed to a threshold voltage shift (with the implicit assumption that the subthreshold characteristics during and after stress remained unchanged from the initial state, which is an assumption that is shown to be valid later in this work). This is depicted in Figure 3. Experiments were performed to monitor charge trapping as a function of gate stress bias polarity, gate bias magnitude, and measurement temperature. All devices measured had a gate width of  $10 \mu\text{m}$  and a gate length of  $\sim 130$  nm.

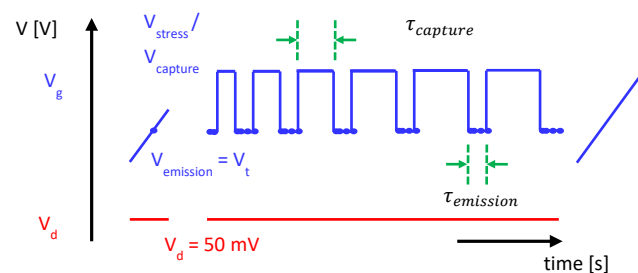


**Figure 3.** Measure–stress–measure sequence applied in this study, incorporating  $I_d$ - $V_g$  measurements in the linear regime after the final sequence.

### 3. Results

#### 3.1. Positive Bias Temperature Instability Results

##### 3.1.1. Charge Trapping

After stressing at positive bias, the threshold voltage was monitored for devices with different GaN channel thickness values (300 nm and 150 nm), and the results are shown in Figure 4. The stress voltage was varied to explore the bias dependence of charge capture and emission. As seen in Figure 4, there are negligible threshold voltage shifts for thick channel devices, but on reducing the channel thickness to 35 nm, negative threshold voltage shifts are seen, which initially display negligible bias dependence and a monotonically reducing maximum  $V_t$  reduction with stress bias after longer stress times. The time dependence is broadly similar in the pre-saturation phase.

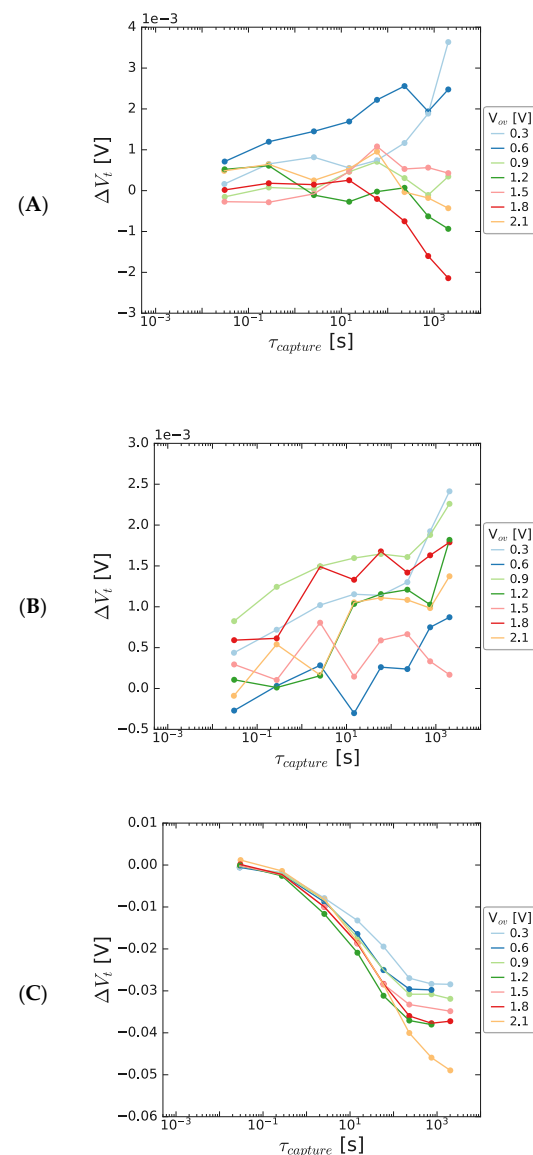


**Figure 4.** Threshold voltage shift as a function of PBTI stress time for a range of overdrive voltage values for HEMT structures, measured at 125 °C, with (A) 300 nm, (B) 150 nm, and (C) 50 nm GaN channel thicknesses.  $V_t$  shift collected 10 ms after end of each stress cycle. The stack contained 8 nm AlGaIn/1 nm AlN/GaN/1  $\mu$ m C-GaN.

The temperature dependence of the PBTI was explored for thin GaN channel samples, and the results are shown in Figure 5. As can be seen, a negative  $V_t$  shift of 40–70 mV

is seen after ~2000 s stress, with a shorter time constant for the onset of the  $V_t$ -reducing mechanism on increasing temperature. An Arrhenius plot of the time constant of the negative  $V_t$  mechanism is shown in (B) and yields an activation energy of ~90 meV.

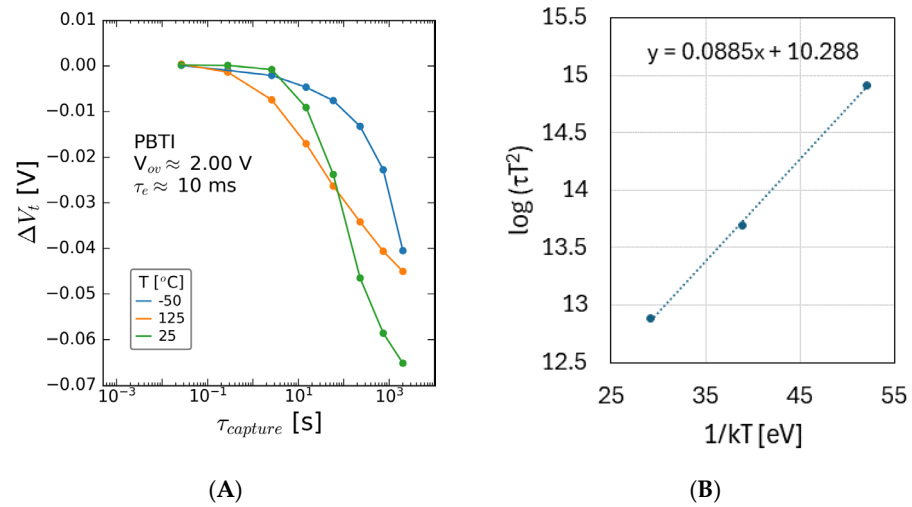


**Figure 5.** Threshold voltage shift as a function of stress time, for multiple temperatures, measured for samples with (A) 35 nm GaN channel and (B) Arrhenius plot for activation energy extraction of negative  $V_t$  mechanism, showing ~90 meV  $E_a$  for the negative  $V_t$  shifting mechanism. The stack contained 8 nm AlGaN/1 nm AlN/35 nm GaN/1  $\mu$ m C-GaN.

The subthreshold characteristics were studied for these structures, to explore the possible link between the AlN/GaN channel surface as the possible origin of the defects responsible for the observed instabilities, and are summarized in Figure 6. There was no clear correlation between subthreshold slope and threshold voltage shift (measured from the final  $I_d$ - $V_g$  curve, i.e., after 2000 s stress and 1000 s relaxation). Similar results were obtained for the other samples, and the results suggest that the measured instabilities are not related to the 2DEG/GaN surface.

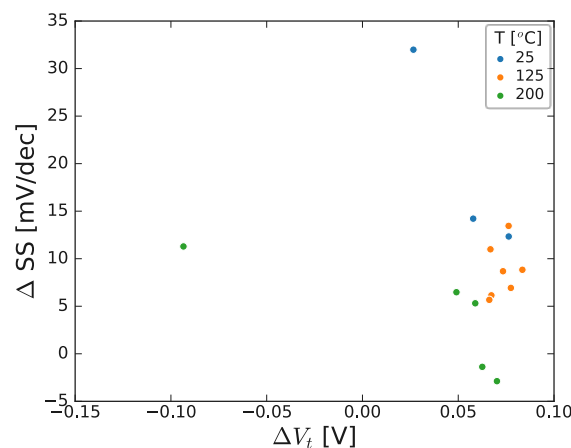


**Figure 6.** Correlation between subthreshold slope and threshold voltage shift for a range of devices, stressed at different stress conditions, and temperatures. Results shown for 300 nm GaN channel. Note each point represents a single device, stressed at a specific stress condition for ~2000 s, and subsequently had ~1000 s relaxation prior to final IV measurement. The stack contained 8 nm AlGaN/1 nm AlN/300 nm GaN/1  $\mu$ m C-GaN.

### 3.1.2. Emission Characteristics after PBTI

After the stress phase, the stability of the drain current was monitored (and any changes were transformed into  $\Delta V_t$ ), by biasing the device at the initial  $V_t$ . The reduction

in the bias condition can enable emission from defects charged during the preceding stress phase and the results are shown for different GaN channel thickness samples in Figure 7. It is shown that, while there is a slightly negative  $V_t$  shift immediately after the stress phase, the subsequent biasing at the initial  $V_t$  results in an increase in the  $V_t$  value to marginally above zero in all cases. The bias dependence of recovery is not particularly strong (<4 mV), with a slightly higher (negative)  $V_t$  shift resulting from the higher bias conditions. It is notable that the magnitude of the  $V_t$  shift is significantly more negative for the 35 nm channel sample (Figure 7C), where the initial negative shift exceeds 60 mV before reducing toward and above zero during the emission phase, clearly demonstrating a strong impact of channel thickness on this negative  $V_t$  shift.

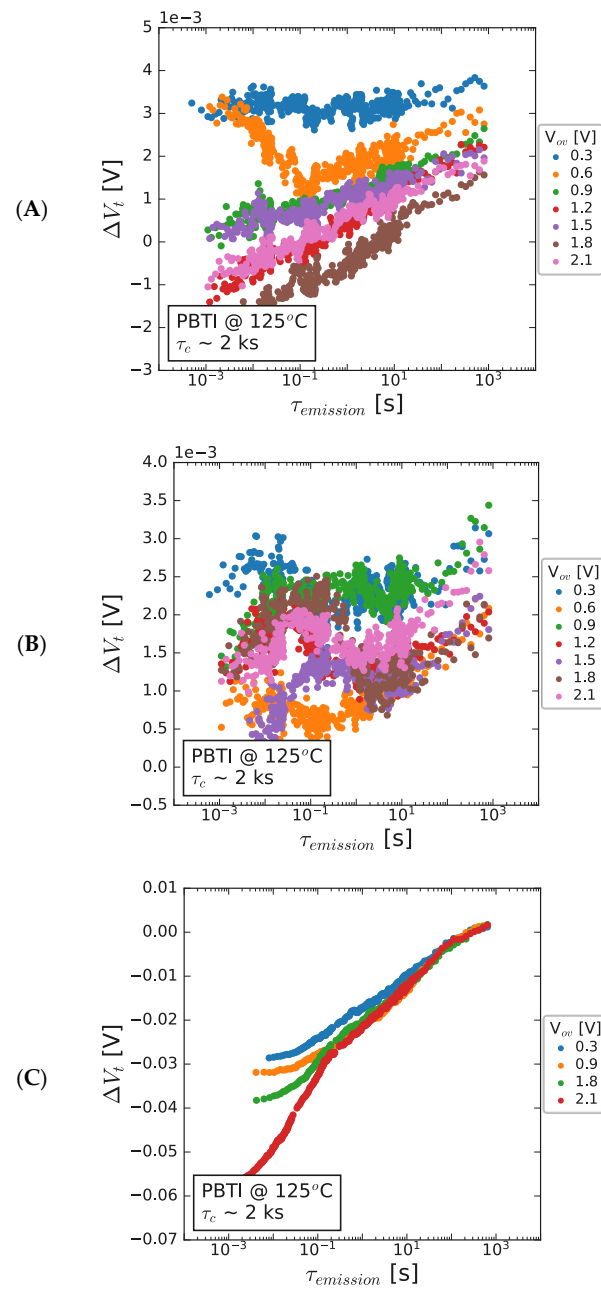


**Figure 7.** Threshold voltage shift as a function of recovery time after PBTI stressing for a range of overdrive voltage values for HEMT structures at 125 °C, with (A) 300 nm (B) 150 nm, and (C) 50 nm GaN channel thickness. The stack contained 8 nm AlGaIn/1 nm AlN/GaN/1  $\mu\text{m}$  C-GaN.

The impact of inserting an AlGaIn back barrier between the C-GaN layer and the GaN channel on the emission behavior is summarized in Figure 8, where the stress time increases from 30 ms to 2000 s on each panel. A negative  $V_t$  shift is seen for the 35 nm GaN sample, with C-GaN back barrier, which is not the case when an AlGaIn back barrier is inserted between the GaN and C-GaN layer. It is noted that the final  $V_t$  shift (i.e., post-emission) is similar in both cases, despite the significant capture and emission process in the C-GaN back-barrier sample. The learning from this is contribution of the C-GaN back barrier to the negative  $V_t$  shift and rapid emission thereafter, and the possibility to screen this effect on insertion of an AlGaIn back barrier.

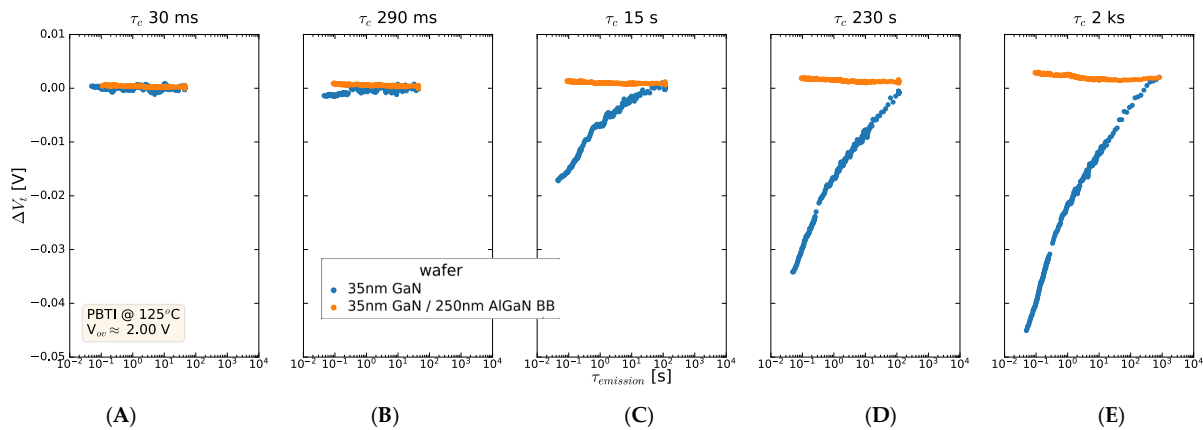


**Figure 8.** Threshold voltage shift as a function of emission time after stressing at times ranging from (A) ~30 ms, (B) 280 ms, (C) 15 s, and (D) 230 s to (E) 2000 s, where the stress was applied at 2.0 V overdrive. The stacks contained 8 nm AlGaIn/1 nm AlN/35 nm GaN/with or without AlGaIn back barrier/1 μm C-GaN.

To summarize the PBTI results on HEMT structures, we see a negative  $V_t$  shift during stress, which shows limited bias dependance. The negative  $V_t$  shift is enhanced by reducing the channel thickness. During the post-stress emission stage, we see an increasing  $V_t$  shift recovering the stress-induced shift, such that a very low (positive)  $V_t$  shift remains after the relaxation stage. This relaxation is also enhanced by reducing the channel thickness and is not related to changes in the interface between the GaN channel and the AlN. The effect can be alleviated for thin channel devices using an AlGaIn back barrier.

### 3.2. Negative Bias Temperature Instability Results

#### 3.2.1. Charge Capture during NBTI

On stressing at negative voltages, i.e. in the OFF-state condition, the  $V_t$  shifts observed in a 150 nm GaN channel sample are summarized in Figure 9.

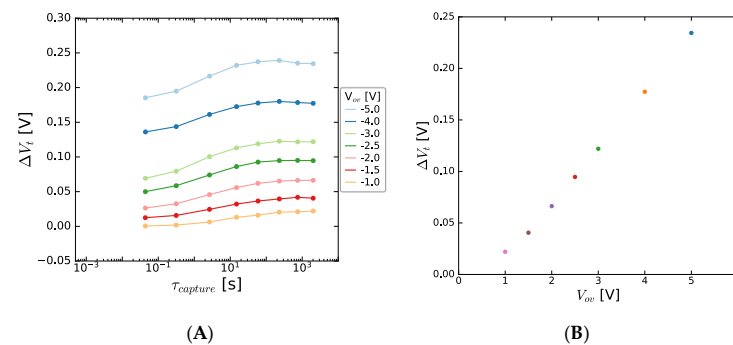


**Figure 9.** Threshold voltage shift seen as a function of (A) NBTI stress time for 150 nm GaN channel HEMT. A positive  $V_t$  shift is seen in (B) which increases linearly with overdrive voltage. The stack contained 8 nm AlGaIn/1 nm AlN/150 nm GaN/1 μm C-GaN.

There is a strong positive  $V_t$  shift seen, which increases with (negative) stress bias. This charge trapping occurs very quickly in the case of high bias, suggesting the trapping in readily accessed defect sites, and when plotted versus the overdrive voltage, a linear trend is seen. In MOSFET BTI structures, this  $V_t$  shift follows a power-law relationship with  $V_{ov}$ , and the power-law exponent is correlated to the accessibility of the responsible defects. For Si/high- $\kappa$  MOSFETs, power-law exponents of three are commonly seen for NBTI. In this case, a power-law exponent of one (i.e., a linear) correlation is seen, suggesting a similarity of energetic alignment between the Fermi level in the 2DEG and the responsible defect level, and thus a defect level that is readily accessible for capture (and emission, as shown later). Given that, during the NBTI, the transistor is biased in the OFF-state, i.e., the 2DEG is switched off, the possible impact of the buffer/back barrier are not screened. In a bid to understand further, the impact of GaN channel thickness is explored and shown to be very pronounced in Figure 10, with an enhanced  $V_t$  shift for the thin channel devices seen.

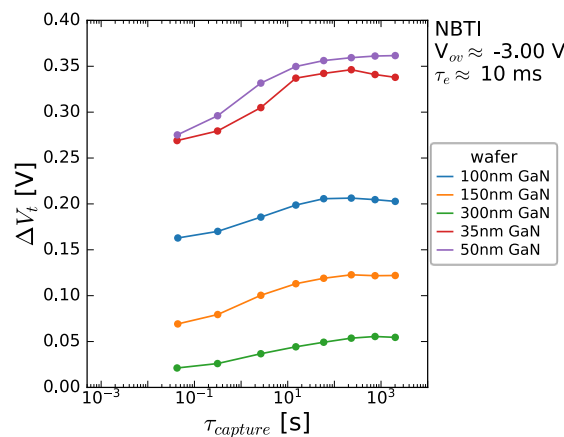


**Figure 10.** Threshold voltage shift seen as a function of stress time for a range of channel thicknesses measured during stressing at  $V_{ov} = -3$  V at 125 °C. The stack contained 8 nm AlGaIn/1 nm AlN/GaN/1  $\mu$ m C-GaN.

It is also noted that, given the degree of variability in the displayed dataset, there is no clear correlation between stress-induced subthreshold slope change and the applied stress bias condition, as demonstrated in Figure 11 and shown after NBTI stress at a range of bias conditions.

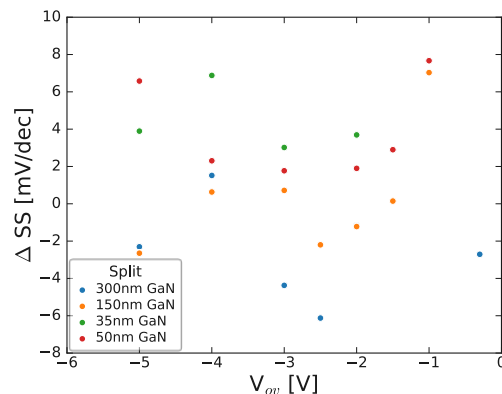


**Figure 11.** Change in subthreshold slope as a function of threshold NBTI stress (overdrive) voltage for a range of HEMTs with varying GaN channel thickness. Note that each point represents a single device stressed at a specific stress condition for  $\sim 2000$  s and, subsequently, had  $\sim 1000$  s relaxation prior to final IV measurement (see next section). The stack contained 8 nm AlGaIn/1 nm AlN/GaN/1  $\mu$ m C-GaN.

### 3.2.2. Post-NBTI Emission

The emission kinetics after NBTI are shown for 50 and 150 nm GaN channel devices in Figure 12. The higher  $V_t$  shifts described in the last section are again present and, in both cases, followed by emission, which begins at  $\sim 10$  ms and before 1 s has fully emitted the trapped charge. While the  $V_t$  shift increases with stress bias, the emission kinetics are independent of stress bias, suggesting the same origin for the responsible defect across all bias conditions and channel thicknesses.

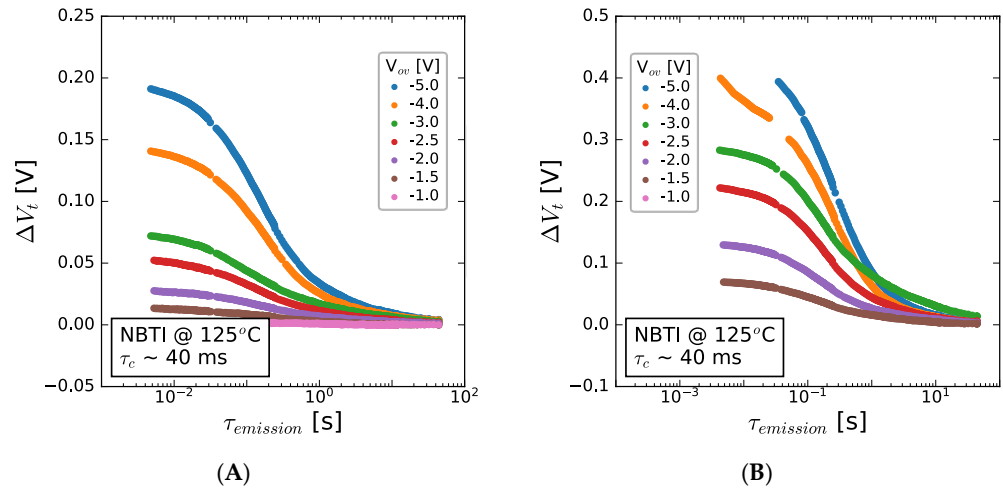


**Figure 12.**  $V_t$  shift seen after NBTI stress at 125 °C at a range of stress bias conditions and as a function of emission time for (A) 150 nm GaN channel and (B) 50 nm GaN channel thickness, with C-GaN back barrier present under the channel in both cases. The stacks contained 8 nm AlGaIn/1 nm AlIn/GaN/1  $\mu$ m C-GaN.

The temperature dependence of the post-NBTI emission is shown in Figure 13 for the 35 nm GaN channel sample, and while the magnitude of the  $V_t$  shift reduces with the temperature, the time constant for the emission process shows strong temperature dependence. This time constant for emission was extracted by the approach detailed in [16]. An Arrhenius plot yields an activation energy of 0.25 eV for the responsible defect.

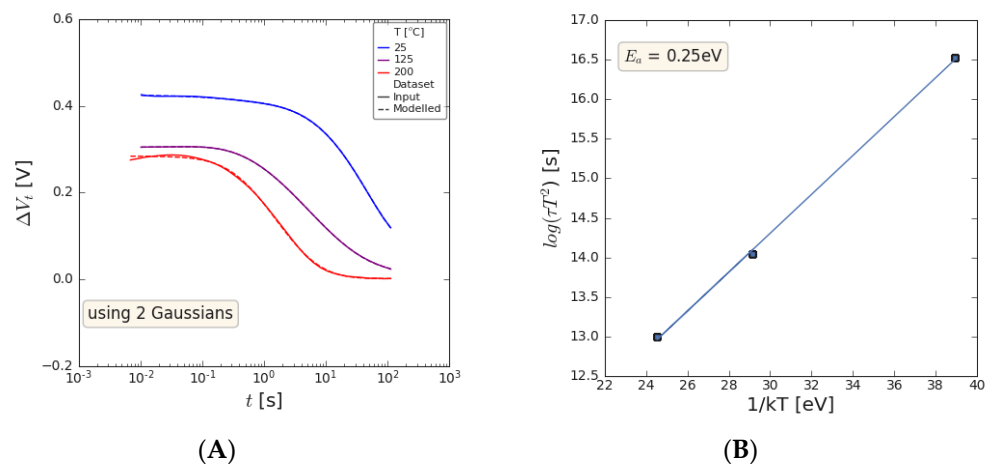


**Figure 13.**  $V_t$  shift seen as a function of (A) emission time for a range of measurement temperatures stressed at  $V_{ov} = -3$  V and (B) Arrhenius plot of time constant for emission behavior shown in (A). Data reported for sample containing 8 nm AlGaIn/1 nm AlIn/35 nm GaN/1  $\mu$ m C-GaN.

The impact of inserting an AlGaIn back barrier between the GaN channel and the C-GaN back barrier is summarized in Figure 14, where the  $V_t$  shifts versus emission time are shown for a range of stress times (on each panel). It is clear that the rapid  $\Delta V_t$  increase

seen in the 35 nm GaN sample is not seen when an AlGaIn back barrier is inserted between the 35 nm GaN channel and the C-GaN. Instead, the AlGaIn back-barrier samples display a slightly negative  $\Delta V_t$  shift, which increases towards and above zero during emission. It is also noted that the trend of the  $V_t$  shift seen in these AlGaIn back-barrier samples is significantly different from that seen with a 150 nm GaN channel (Figure 12A). This clearly shows the impact of AlGaIn screening the effect of this  $V_t$  shift, which is effective for the very significant shifts seen in the thin GaN channel devices.

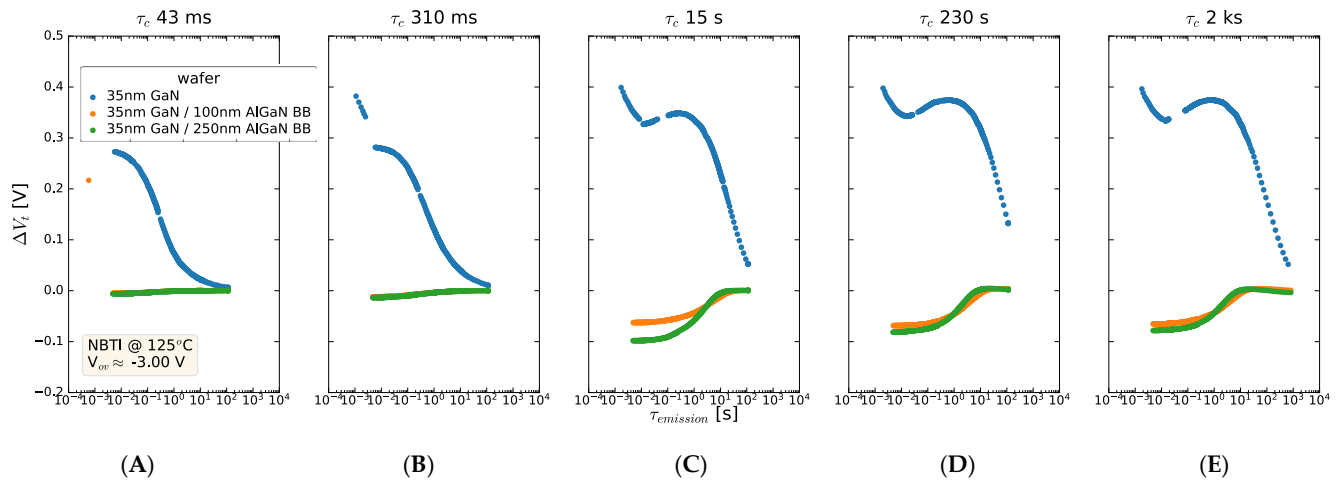


**Figure 14.** Threshold voltage shift as a function of emission time after stressing at times ranging from (A) ~30 ms, (B) 280 ms, (C) 15 s, and (D) 230 s to (E) 2000 s, where the stress was applied at  $-2.0$  V overdrive. A positive  $V_t$  shift is seen for the 35 nm GaN sample and emission with a characteristic time constant, whereas when an AlGaIn back barrier is inserted between the GaN and C-GaN layer, the positive  $V_t$  shift is not seen. The stack contained 8 nm AlGaIn/1 nm AlN/GaN/0–250 nm AlGaIn back barrier/1  $\mu\text{m}$  C-GaN.

To summarize the NBTI results, positive  $V_t$  shifts are seen due to negative bias stress, with increasing magnitude with (negative) bias and downscaling the channel thickness. These  $V_t$  shifts are recovered during the subsequent emission phase and show no correlation with the GaN/AlGaIn interface characteristics. The time constant for the emission process shows temperature dependence and can be described by the Arrhenius relationship, with an activation energy of 0.25 eV. The positive threshold voltage shift can be effectively screened by the insertion of an AlGaIn back barrier, with no positive  $V_t$  shift seen with 100 nm AlGaIn between the C-GaN back barrier and the 35 nm GaN channel.

#### 4. Discussion

The previous sections have presented data collected after stressing Schottky gate HEMT structures, under positive and negative bias, as a function of stress time, stress bias, temperature, and GaN channel thickness. It was shown that a negative  $V_t$  shift was seen after PBTI, whereas a positive shift was seen after NBTI, both of which were anomalous when compared to the MOSFET gate dielectric reliability observations. The  $V_t$  shifts reduced during a subsequent post-stress emission stage, (at  $V_t$  for both polarities). There were negligible changes in the subthreshold characteristics for both stress polarities, suggesting that defect creation at the GaN/AlN interface is not related, and the relaxation of the  $V_t$  shift suggests that these processes are a capture/emission related process, from pre-existing defects in the stack.

To help understand the bias distribution across the constituent layers in these complex stacks, the band diagram was simulated and is shown in Figure 15. In this case, for the 35 nm GaN channel, the underlying C-GaN back barrier is also included in the figure. The role of this C-GaN back barrier needs to be considered. The widely reported C-acceptor level at  $E_v + 0.9$  eV [8] becomes relevant for these structures and at the considered biasing

conditions. The blue dotted lines show the energetic alignment of the C-acceptor level in the unintentionally doped GaN and predominantly C-GaN layers, while the red line shows the energetic alignment of the Fermi level at 0.25 eV above  $E_{c \text{ min}}$  GaN, using the activation energy value calculated from Figure 13B. The close energetic alignment of the deep levels in the C-GaN and the 2DEG is clearly seen and can explain the  $V_t$  shift seen during the emission phase after NBTI, whereas trapping from the gate, directly in the C-GaN defect levels, is believed to be responsible for the positive  $V_t$  shifts seen in these GaN HEMT structures.

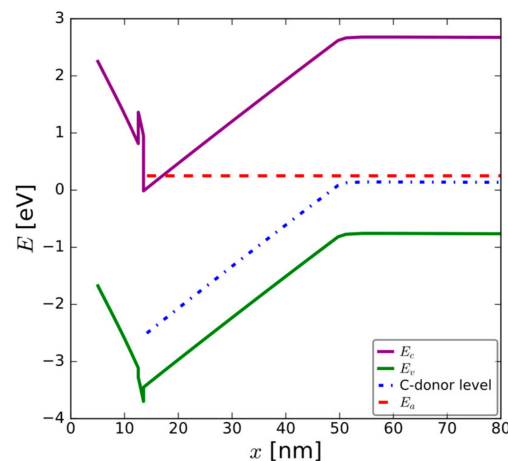


**Figure 15.** Calculated energy-band diagram for 35 nm GaN channel biased at the threshold condition. Note the energetic alignment between the C-acceptor level in the C-GaN back barrier and the Fermi level. Simulated stack contained 8 nm AlGaIn/1 nm AlN/35 nm GaN/1  $\mu\text{m}$  C-GaN.

During the stress phase, as mentioned previously, for a device biased in the OFF state, there is no 2DEG, so it cannot contribute to any charge trapping. Given that increased charging is observed for a thinner GaN, it is, therefore, believed that this charging results from electron injection directly from the gate electrode to the C-GaN back barrier layer, which can subsequently be emitted to the channel on reducing the bias from the stress voltage to the emission voltage, (or initial  $V_t$ ), as depicted in Figure 14. The negative  $V_t$  shifts due to PBTI, result from electrons being collected in the 2DEG from the C-GaN levels, which are located at higher levels energetically under these bias conditions. That the shifts are lower in the case of PBTI than NBTI is believed to be related to the lower electrical communication between the C-GaN levels and the 2DEG when the device is switched ON.

The  $V_t$  instabilities in these Schottky gate structures are believed to be related to the carbon-doping levels in the C-GaN back barrier. Efforts to place this layer further from the channel by increasing the channel thickness are seen to limit the charge trapping for BTI stressing at either positive or negative polarities (Figures 4 and 10, respectively), albeit at a cost of a lower threshold voltage. Insertion of an AlGaIn back barrier is shown to reduce NBTI (significantly) and PBTI (significantly) with the compromise of increased thermal resistance to dissipate the generated heat during operation [7].

## 5. Conclusions

This study reports on experiments performed on the bias temperature instability of Schottky gate HEMT structures for applications as power amplifiers in RF/mm wave communication systems. It is shown that the threshold voltage shifts during bias temperature instability measurements, with positive  $V_t$  shifts during NBTI and negative  $V_t$  shifts during PBTI. Both the positive and negative shifts reduce during a post-stress subsequent emission step. Neither the positive nor the negative  $V_t$  shifts are correlated with changes in the GaN/AlN interface characteristics, leading to the conclusion that the cause is capture and emission in pre-existing defect levels within the AlGaIn/AlN/GaN/C-GaN stacks. The energy-band diagram suggests direct access between the Fermi level in the 2DEG at  $V_t$

and the dopant level in the C-doped GaN back barrier. The bias induced band diagram modulation and enabled access to and from this defect level for both biasing conditions.

**Author Contributions:** Methodology, B.O.; Writing—original draft, B.O.; Writing—review & editing, A.R., A.A., S.Y., H.Y., A.S.-H., U.P., B.P., A.C. and N.C. All authors have read and agreed to the published version of the manuscript.

**Funding:** This work was performed in the framework of the imec Advanced RF program.

**Data Availability Statement:** The data presented in this study may be available on request from the corresponding author.

**Conflicts of Interest:** All authors were employed by the company IMEC. The remaining authors declare that the research was conducted in the absence of any commercial or financial relationships that could be construed as a potential conflict of interest.

## References

- Collaert, N.; Alian, A.; Banerjee, A.; Boccardi, G.; Cardinael, P.; Chauhan, V.; Desset, C.; ElKashlan, R.; Khaled, A.; Ingels, M.; et al. III-V/III-N technologies for next generation high capacity wireless communication. In Proceedings of the 2022 International Electron Devices Meeting (IEDM), San Francisco, CA, USA, 3–7 December 2022. [CrossRef]
- Available online: <https://www.researchandmarkets.com/reports/5956562/gan-substrate-market-size-market-share> (accessed on 22 July 2024).
- Chen, X.; Yang, X.; Xie, X.; Peng, Y.; Xiao, L.; Shao, C.; Li, H.; Hu, X.; Xu, X. Research progress of large size SiC single crystal materials and devices. *Light Sci. Appl.* **2023**, *12*, 28. [CrossRef] [PubMed]
- Then, H.W.; Radosavljevic, M.; Koirala, P.; Thomas, N.; Nair, N.; Ban, I.; Talukdar, T.; Nordeen, P.; Ghosh, S.; Bader, S.; et al. Advanced Scaling of Enhancement Mode High-K Gallium Nitride-on-300mmSi(111) Transistor and 3D Layer Transfer GaN-Silicon Finfet CMOS Integration. In Proceedings of the IEEE International Electron Devices Meeting (IEDM), San Francisco, CA, USA, 11–16 December 2021. [CrossRef]
- Then, H.W.; Radosavljevic, M.; Yu, Q.; Latorre-Rey, A.; Vora, H.; Bader, S.; Momson, I.; Thomson, D.; Beumer, M.; Koirala, P.; et al. Enhancement-Mode 300-mm GaN-on-Si(111) with Integrated Si CMOS for Future mm-Wave RF Applications. *IEEE Microw. Wirel. Technol. Lett.* **2023**, *33*, 835–838. [CrossRef]
- Bisi, D.; Meneghini, M.; de Santi, C.; Chini, A.; Dammann, M.; Brückner, P.; Mikulla, M.; Meneghesso, G.; Zanoni, E. Deep-Level Characterization in GaN HEMTs-Part I: Advantages and Limitations of Drain Current Transient Measurements. *IEEE Trans. Electron Devices* **2013**, *60*, 3166–3175. [CrossRef]
- Vermeersch, B.; Rodriguez, R.; Sibaja-Hernandez, A.; Vais, A.; Yadav, S.; Parvais, B.; Collaert, N. Thermal Modelling of GaN & InP RF Devices with Intrinsic Account for Nanoscale Transport Effects. In Proceedings of the 2022 International Electron Devices Meeting (IEDM), San Francisco, CA, USA, 3–7 December 2022; pp. 15.3.1–15.3.4. [CrossRef]
- Reshchikov, M.A.; Vorobiov, M.; Demchenko, D.O.; Özgür, Ü.; Morkoç, H.; Lesnik, A.; Hoffmann, M.P.; Hörich, F.; Dadgar, A.; Strittmatter, A. Two charge states of the  $C_N$  acceptor in GaN: Evidence from photoluminescence. *Phys. Rev. B* **2018**, *98*, 125207. [CrossRef]
- Gao, Z.; Chiochetta, F.; De Santi, C.; Modolo, N.; Rampazzo, F.; Meneghini, M.; Meneghesso, G.; Zanoni, E.; Blanck, H.; Stieglauer, H. Deep level effects and degradation of 0.15  $\mu\text{m}$  RF AlGaIn/GaN HEMTs with Mono-layer and Bi-layer AlGaIn backbarrier. In Proceedings of the IEEE International Reliability Physics Symposium, Dallas, TX, USA, 27–31 March 2022. [CrossRef]
- Uren, M.J.; Kuball, M. Current collapse and kink effect in GaN RF HEMTs: The key role of the epitaxial buffer. In Proceedings of the 2020 IEEE BiCMOS and Compound Semiconductor Integrated Circuits and Technology Symposium (BCICTS), Monterey, CA, USA, 16–19 November 2020; pp. 1–8. [CrossRef]
- Cioni, M.; Zagni, N.; Iucolano, F.; Moschetti, M.; Verzellesi, G.; Chini, A. Partial Recovery of Dynamic RON Versus OFF-State Stress Voltage in p-GaN Gate AlGaIn/GaN Power HEMTs. *IEEE Trans. Electron Devices* **2021**, *68*, 4862. [CrossRef]
- Zanoni, E.; Rampazzo, F.; De Santi, C.; Gao, Z.; Sharma, C.; Modolo, N.; Verzellesi, G.; Chini, A.; Meneghesso, G.; Meneghini, M. Failure Physics and Reliability of GaN-Based HEMTs for Microwave and Millimeter-Wave Applications: A Review of Consolidated Data and Recent Results. *Phys. Status Solidi A* **2022**, *219*, 2100722. [CrossRef]
- Viey, A.G.; Vandendaele, W.; Jaud, M.-A.; Gerrer, L.; Garros, X.; Cluzel, J.; Martin, S.; Krakovinsky, A.; Biscarrat, J.; Gwoziecki, R.; et al. Carbon-related pBTI degradation mechanisms in GaN-on-Si E-mode MOSc-HEMT. In Proceedings of the 2020 International Electron Devices Meeting (IEDM), San Francisco, CA, USA, 12–18 December 2020. [CrossRef]
- Srinivasan, P.; Guarin, F. CMOS RF reliability for 5G mmWave applications—Challenges and Opportunities. In Proceedings of the IEEE International Reliability Physics Symposium (IRPS), Monterey, CA, USA, 21–25 March 2021. [CrossRef]

15. Alian, A.; Rodriguez, R.; Yadav, S.; Peralagu, U.; Hernandez, A.S.; Putcha, V.; Zhao, M.; ElKashlan, R.; Vermeersch, B.; Yu, H.; et al. Impact of channel thickness scaling on the performance of GaN-on-Si RF HEMTs on highly C-doped GaN buffer. In Proceedings of the IEEE European Solid-State Device Research Conference (ESSDERC), Milan, Italy, 19–22 September 2022. [[CrossRef](#)]
16. Putcha, V.; Cheng, L.; Alian, A.; Zhao, M.; Lu, H.; Parvais, B.; Waldron, N.; Linten, D.; Collaert, N. On the impact of buffer and GaN-channel thickness on current dispersion for GaN-on-Si RF/mm-Wave devices. In Proceedings of the 2021 IEEE International Reliability Physics Symposium (IRPS), Monterey, CA, USA, 21–25 March 2021; pp. 1–8. [[CrossRef](#)]

**Disclaimer/Publisher’s Note:** The statements, opinions and data contained in all publications are solely those of the individual author(s) and contributor(s) and not of MDPI and/or the editor(s). MDPI and/or the editor(s) disclaim responsibility for any injury to people or property resulting from any ideas, methods, instructions or products referred to in the content.